JASA ARTICLE

Numerical study of the scattering of acoustic waves by an elliptic vortex

L. Martin-Martin,[1,2,a] V. Clair,[1] C. Bogey,[3] and G. Gabard[4]

[1]*Ecole Centrale de Lyon, CNRS, Universite Claude Bernard Lyon 1, INSA Lyon, Laboratoire de Mécanique des Fluides et d'Acoustique, UMR 5509, Ecully 69130, France*

[2]*Siemens Digital Industries Software, Châtillon 92320, France*

[3]*CNRS, Ecole Centrale de Lyon, INSA Lyon, Universite Claude Bernard Lyon 1, Laboratoire de Mécanique des Fluides et d'Acoustique, UMR 5509, Ecully 69130, France*

[4]*Laboratoire d'Acoustique de l'Université du Mans (LAUM), UMR 6613, Institut d'Acoustique - Graduate School (IA-GS), CNRS, Le Mans Université, Le Mans 72000, France*

ABSTRACT:

The scattering of the acoustic waves generated by a monopolar source propagating through a two-dimensional elliptic vortex, fixed or convected by a uniform flow, is studied by solving the Linearized Euler Equations in Cartesian coordinates using the Discontinuous Galerkin Method. For a fixed vortex position, the number, amplitudes, and angular spreads of the acoustic interference beams resulting from the sound scattering are found to significantly depend on the orientation of the vortex major axis with respect to the direction of the incident waves and on the vortex maximum tangential velocity. In particular, additional interference beams are obtained at large observation angles for a more elliptical vortex. For a convected elliptic vortex, the interference beams are curved as the angle between the incident acoustic wave and the vortex major axis varies when the vortex travels in the downstream direction. As expected, the scattering of the acoustic waves leads to spectral broadening in this case. Moreover, the widths and the frequencies of the lateral lobes obtained in the spectra on both sides of the peak at the source frequency are different for elliptic and round vortices. © *2024 Acoustical Society of America*.

https://doi.org/10.1121/10.0025138

(Received 22 September 2023; revised 14 February 2024; accepted 17 February 2024; published online 1 March 2024)

[Editor: Con Doolan] Pages: 1707–1718

I. INTRODUCTION

During measurements in open wind tunnels, the sound generated inside the flow passes through a turbulent shear layer before reaching the microphones placed in the far field. When acoustic waves propagate through a volume of turbulence such as a jet shear layer, the propagation is modified by the inhomogeneities in the medium properties, leading to spatial scattering. If the volume of turbulence is convected, the sound scattered by the inhomogeneities is affected by a Doppler effect, which leads to spectral broadening. This phenomenon was first studied by Candel *et al.*[1–3] In many instances, for a harmonic source, the resulting acoustic spectra exhibit a peak at the source frequency, with a lower amplitude compared to the peak that would be obtained without scattering, and sidelobes around the peak**. Therefore, the sound properties change as the waves exit the flow, which complicates the analysis of the sources from the data obtained in the far acoustic field. Therefore, a better understanding of this scattering phenomenon would help in interpreting the data.

The modelling of a turbulent mixing layer is complex. It can be achieved numerically, for example through direct numerical simulation, but at a high computational cost. Alternatives exist, such as large eddy simulations,[4] where only the largest turbulent scales are resolved, or stochastic methods such as the random particle-mesh method (RPM),[5] where a turbulent field is synthesized from its statistical properties. In previous work,[1–4] it was shown that the sound scattering in jet flows was mostly due to the contribution of the most energetic eddies in the shear layer. Thus, general properties of spectral broadening can be understood by considering only the most energetic eddies instead of all the turbulent scales.[6] These structures happen to be arranged as an array of equally spaced vortices, convected in the jet shear layers. When the acoustic wavelength is smaller than the vortex size, the interactions of the acoustic wave and the vortex mainly affect the sound field in the source-to-vortex direction.[14] Thus, the sound field scattered by a single vortex interacts with neighbouring vortices when the incidence angle of the acoustic wave is almost parallel to the shear layer. In the literature on sound scattering and spectral broadening,[1–3,26] in most cases the jets have low Mach numbers, the source radiates at a high frequency, and the acoustic measurements are made near the sideline of the source far from the shear layer. Under these assumptions, the vortices do not encounter acoustic perturbations caused by other vortices. Therefore, the scattering induced by each vortex of

[a]Email: laura.martin@ec-lyon.fr

the array does not depend on the other vortices and the scattered field generated by the array of eddies can be considered as the sum of the scattered field of each eddy. As single eddy configurations cannot be easily reproduced experimentally, the sound scattering by a single vortex has been studied in previous work using analytical models[7–11] and simulations.[7,12–17] The eddies can be considered as temperature disturbances, velocity disturbances, or both. A few studies have dealt with the sound scattering for non-isothermal structures,[8,16] but the majority are concerned with velocity disturbances only. In that second case, when a single vortex was considered, it was circular.[7,9,17] However, in mixing layers, the eddies are slightly elongated in the axial direction.[18]

Therefore, the present work aims to explore the scattering of sound waves by a single elliptic vortex by solving the linearized Euler equations (LEE). In this work, a Kirchhoff vortex model is considered as it can be defined analytically in a parametric way. The effects of several parameters such as the aspect ratio and the orientation of the vortex, which are unique to the elliptic vortex, are investigated. The influence of the maximum tangential velocity of the vortex and the ratio between the acoustic wavelength and the vortex size is also studied. Finally, the sound scattering is examined for a fixed elliptic vortex and an elliptic vortex convected by a uniform mean flow.

This article is structured as follows. The parameters of the Kirchhoff vortex are presented in Sec. II. The configuration used in the numerical simulations is described in Sec. III. In Sec. IV, the effects of each parameter defining a fixed elliptic vortex are presented. The case of a vortex convected by a uniform flow is studied in Sec. V. Finally, concluding remarks are provided in Sec. VI.

II. VORTEX DEFINITION

The elliptic vortex chosen in this study was proposed by Kirchhoff.[19] The vortex parameters are represented in Fig. 1. The major and minor semi-axes lengths of the vortex are equal to $a = r_0(1+\epsilon)$ and $b = r_0(1-\epsilon)$, where ϵ quantifies the degree of ellipticity and r_0 is the radius of the corresponding round vortex obtained for $\epsilon = 0$. The aspect ratio of the vortex is defined by a/b. When the vortex is not round, the extremities of the core of the vortex on both sides of its major axis are named vertices of the vortex. The orientation of the major axis with respect to the direction of the acoustic waves passing through the vortex center is characterized by the angle θ. The core of the vortex, in gray, is the region D_θ where the vorticity Ω is uniform. It is defined as

$$D_\theta = \Big\{(r,\gamma)\ \big|[r\cos(\gamma-\theta-\pi/4)/a]^2 + [r\sin(\gamma-\theta-\pi/4)/b]^2 \le 1\Big\}, \tag{1}$$

where (r,γ) are polar coordinates.[20] The vortex induces velocity fields u_0 and v_0 in the Cartesian directions x and y, respectively, while the pressure and density fields are

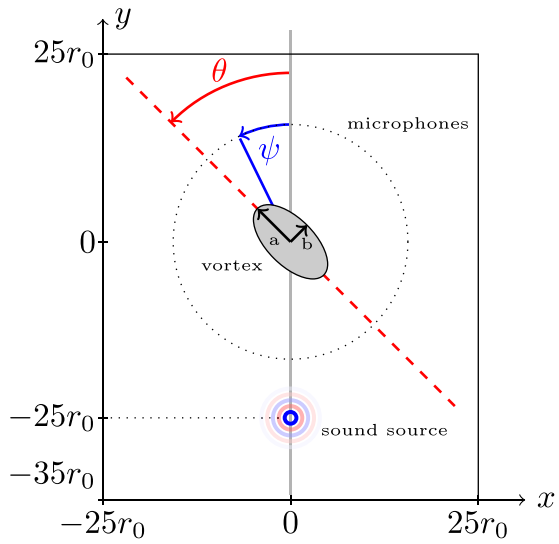

FIG. 1. (Color online) Numerical configuration for the vortex at a fixed position. Only the physical domain is shown.

constant. For simplicity, the expression of the velocity field is formulated through the stream function ϕ such that $u_0 = -\partial\phi/\partial y$, $v_0 = \partial\phi/\partial x$. The definition of the stream function is different inside and outside the core of the vortex,

$$\phi = \begin{cases} \dfrac{\Omega}{2(a+b)}\Big[b(r\cos(\gamma-\theta-\pi/4))^2 \\ \quad + a(r\sin(\gamma-\theta-\pi/4))^2\Big] & \text{if}(r,\gamma)\in D_\theta, \\ \dfrac{\Omega ab}{4}\cos(2(\gamma-\theta-\pi/4))e^{-2\cosh^{-1}\left(r/\sqrt{a^2-b^2}\right)} \\ \quad + \dfrac{\Omega ab}{4}2\cosh^{-1}\left(\dfrac{r}{\sqrt{a^2-b^2}}\right) & \text{if}(r,\gamma)\notin D_\theta. \end{cases} \tag{2}$$

This expression is deduced from the paper of Barré.[20] The resulting velocity field is continuous, but not differentiable at the boundary of D_θ. This can be observed in Fig. 2, where the horizontal velocity u_0 of a round vortex ($a/b = 1$) is plotted along $x = 0$. The velocity evolves linearly inside the core of the vortex, shown in gray, and non-linearly outside. The maximal tangential velocity of the vortex is reached at the boundary of D_θ. It is given by $U_v = M_v c_0 = ab\Omega/(a+b)$, where M_v is the vortex Mach number associated with the velocity U_v, and c_0 is the speed of sound in the ambient medium.

In Sec. V, the vortex will be convected in the axial direction by a uniform mean flow with a velocity $U_c = M_c c_0$, where M_c is the convection Mach number. In that case, the velocity field will be the sum of the convection velocity and the vortex velocity with the vortex position evolving in time due to the convection.

III. NUMERICAL PARAMETERS

In this study, a monopolar acoustic source is considered, placed below the elliptic vortex as shown in Fig. 1, whose radiated field is scattered by the vortex. The acoustic

https://doi.org/10.1121/10.0025138

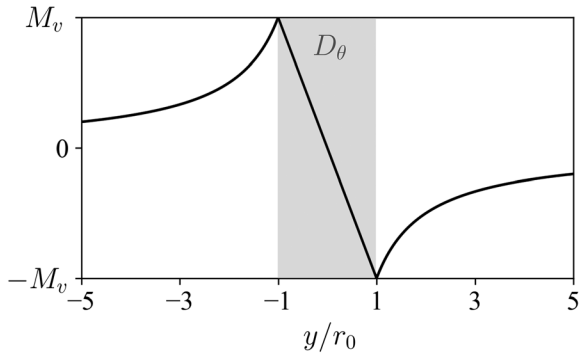

FIG. 2. Profile of axial velocity u_0/c_0 for a round Kirchhoff vortex at $x = 0$.

field is computed by solving the linearized Euler equations written with the Goldstein pressure π',[21] using a research code provided by Siemens. The code is based on the nodal discontinuous Galerkin method[22,23] with polynomial order $N = 4$, and a 6-stage, optimized, low-storage Runge-Kutta scheme.[24] The accuracy of the code when the acoustic waves propagate in a uniform base flow has been assessed previously in the literature.[25] The validity of the code for the scattering of sound has been verified by simulating the scattering of acoustic plane waves by a Gaussian round vortex. The results were in excellent agreement with those from the literature.[14] It can be noted that the Kirchhoff vortex does not verify the LEE. This results in the presence of source terms on the right-hand side of the equations, that may generate spurious acoustic waves. The amplitude of these spurious waves in the present work has, however, been checked to be negligible compared with that of the waves radiated by the monopole source.

The positions of the vortex and the monopole within the physical region of the computational domain are represented in Fig. 1 when the vortex is fixed in space. The vortex is centered on (0, 0) in this case. The monopole is introduced through source terms on the right-hand side of the LEE

$$\begin{cases} s_{\rho'}(x,y) = \rho_0 \sin(\omega_0 t) \exp\left(-\dfrac{(x-x_c)^2 + (y-y_c)^2}{b_m^2}\right), \\ s_{(\rho u)'}(x,y) = s_{\rho'}(x,y) u_0(x,y), \\ s_{(\rho v)'}(x,y) = s_{\rho'}(x,y) v_0(x,y), \\ s_{\pi'}(x,y) = \dfrac{\pi_0(x,y)}{\rho_0(x,y)} s_{\rho'}(x,y), \end{cases} \tag{3}$$

where $x_c = 0$, $y_c = -25r_0$ is the center of the monopole, and ω_0 is the angular frequency. The wavelength of the acoustic wave is $\lambda_0 = 2\pi c_0/\omega_0$ and the Gaussian half-width b_m is $r_0/10$. The choice of a monopolar source leads to curved acoustic waves. Then, the wavelength and the angle of incidence of the acoustic waves reaching the vortex depend on the position of the vortex and the mean flow velocity.

The physical domain extends over $-25r_0 \le x \le 25r_0$ and $-35r_0 \le y \le 25r_0$, and a buffer zone with a width of $5r_0$ is added on each side of the computational domain. An unstructured triangular mesh is used. The average length of the side of the elements in the physical domain is h, and the distance between nodes is $\Delta = h/4$ for a polynomial order $N = 4$. The size of the elements h is chosen to ensure at least ten nodes per λ_0 and r_0 in all cases because the code requires at least seven nodes per λ_0 to propagate waves accurately. The ratio between the acoustic wavelength and the vortex size λ_0/r_0 takes different values between 1/4 and 4. Therefore, three meshes are considered, with $\Delta = r_0/40$, $r_0/20$ and $r_0/10$, depending on λ_0/r_0. The time step Δt is chosen so that

$$CFL = \Delta t \max_{e \in \text{mesh}} \left\{ \frac{u_{e,max}}{\Delta_{norm} R_e} \right\} \simeq 0.9,$$

where $u_{e,max}$ is the maximal phase speed in the element e, Δ_{norm} is the smallest distance between nodes of a normalized element of side $h = 1$, and R_e is the radius of the inscribed circle in the element e.[23] The element size at the outer boundary of the buffer zone h_{out} is twice the element size inside the physical domain. This difference in size is obtained using a stretching of the mesh inside the buffer zone, which is combined with a dissipative high-order filtering procedure (see section 5.3 in Hesthaven and Warburton[22]) The filter intensity varies linearly between the inner and outer boundaries of the buffer zone, cancelling the terms of high order near the outer border. A high-order filter is also applied everywhere in the domain with a cut-off order $N_c = N - 1$. In practice, the terms of order N are cancelled at each time step.

When the position of the vortex is fixed, the pressure is recorded on microphones located at a distance of $10r_0$ of the center of the vortex, as shown in Fig. 1. The angle indicating the microphone position is denoted ψ.

When the vortex is convected by a uniform flow, the mesh with $\Delta = r_0/10$ is used. However, it is longer than previously and extends between $-75r_0 \le x \le 75r_0$ for its physical part, as represented in Fig. 3. This allows the vortex to travel over a large distance. Only three microphones, located at $x/r_0 = -30$, 0, 30 and $y/r_0 = 16$ are considered in this case.

IV. VORTEX AT A FIXED POSITION

In this section, the position of the vortex is fixed at (0, 0). There is no Doppler effect in this case since there is no relative

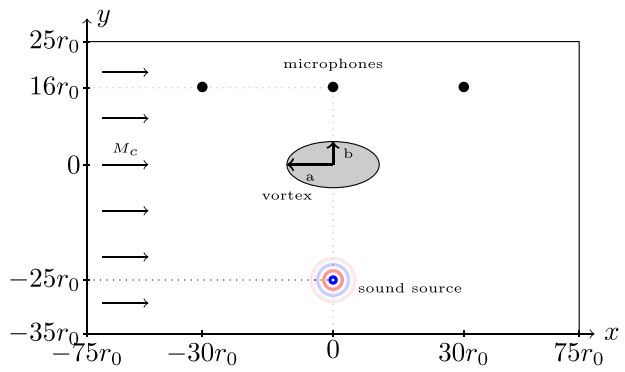

FIG. 3. (Color online) Numerical configuration for the convected vortex. Only the physical domain is shown.

motion between the source, the vortex, and microphones. Thus, only the spatial scattering of the acoustic waves is examined.

A. Influence of the vortex aspect ratio *a* / *b*

The effects of the vortex aspect ratio a/b on the sound spatial scattering are investigated for values of a/b ranging from 1, for which the vortex is round, to 5. The other parameters, such as the vortex Mach number $M_v = 0.15$ and the acoustic wavelength $\lambda_0/r_0 = 1$ are fixed. A vortex orientation of $\theta = \pi/4$ is chosen because it allows to observation of several strong interference beams over a wide range of observation angles, as will be shown in the next section in Fig. 7.

Instantaneous pressure fields are presented in Fig. 4 for, $a/b = 1, 2, 3$, and 5. Beams of high and low intensities can be seen above the vortex. They are created by the constructive and destructive interferences between the acoustic waves scattered by the vortex and the waves coming directly from the source. More beams are visible on the left of the vortex than on the right. The beams close to $\psi = 0$ are also more marked than the ones found at large values of ψ. The angular positions of the beams do not seem to significantly change with the vortex aspect ratio, but their number clearly increases as the vortex becomes more elongated.

The sound scattering is quantified by the normalized difference between the root mean square pressure values obtained at $10r_0$ from the vortex with and without the vortex $|p'_{rms} - p'_{ref,rms}|/p'_{ref,rms}$. This quantity is shown in Fig. 5 as a function of the ratio a/b and of the observation angle ψ. Horizontal stripes are observed. They correspond to the interference beams visible in the pressure fields of Fig. 4. As expected, given the latter figure, the stripes are nearly all found for $\psi > 0$, and the widest and most intense ones are located near $\psi = 10°$. Moreover, as the vortex aspect ratio is larger, the angular positions of the stripes do not vary appreciably but their amplitudes slightly increase. Additional stripes also appear progressively for large angle ψ as the value of a/b increases.

To explain these trends, the ray tracing method is implemented to compute the paths followed by the acoustic rays as they propagate. One hypothesis in this method is that the acoustic source emits at a very high frequency. This will most likely lead to differences between the LEE and the ray tracing results, as will be discussed later. The acoustic rays are obtained by solving the equations given in Candel,[12]

$$\left(\frac{\partial x}{\partial t}, \frac{\partial y}{\partial t}\right) = c_0 \frac{(k_x, k_y)}{k} + (u_0, v_0), \tag{4}$$

$$\left(\frac{\partial k_x}{\partial t}, \frac{\partial k_y}{\partial t}\right) = -k\nabla c_0 - (k_x, k_y)\begin{pmatrix} \frac{\partial u_0}{\partial x} & \frac{\partial u_0}{\partial y} \\ \frac{\partial v_0}{\partial x} & \frac{\partial v_0}{\partial y} \end{pmatrix}, \tag{5}$$

where (k_x, k_y) is the wave vector, and k its norm. The equations are solved using a 4-stage Runge-Kutta method.

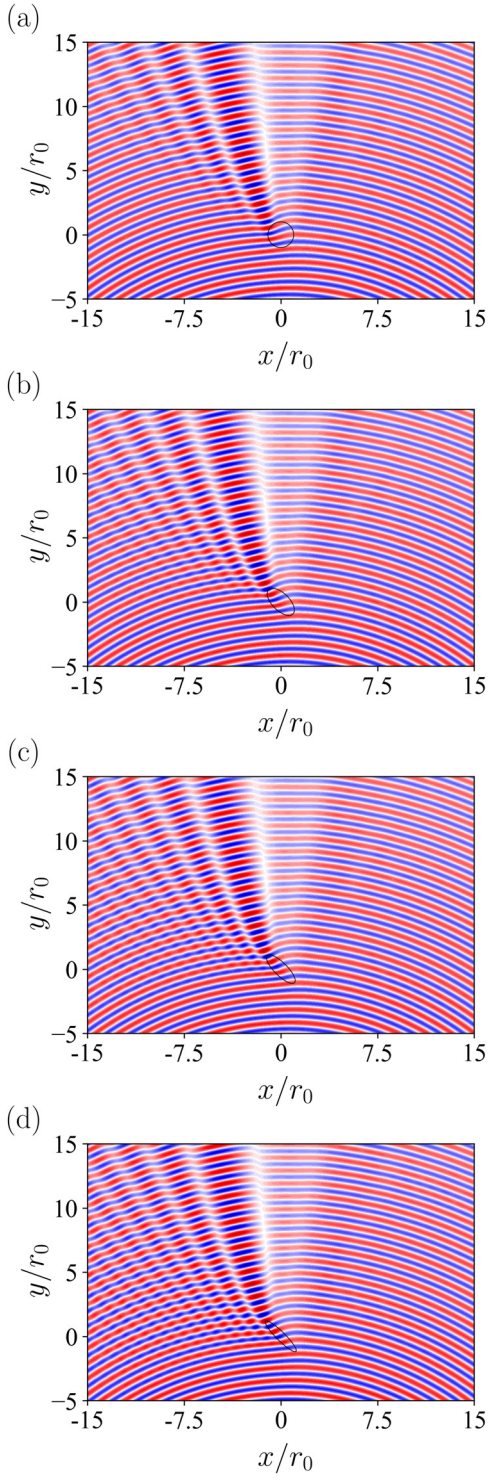

FIG. 4. (Color online) Pressure fields p' obtained for (a) $a/b = 1$, (b) $a/b = 2$, (c) $a/b = 3$, and (d) $a/b = 5$ for a vortex with an orientation angle $\theta = \pi/4$, a maximal Mach number $M_v = 0.15$, and for an acoustic wavelength $\lambda_0/r_0 = 1$.

In practice, 18 rays are launched from the monopole position toward the vortex, with initial directions ranging from $-\pi/20$ to $\pi/20$ relative to the vertical direction, as can be seen in Fig. 6.

The rays obtained for $a/b = 1$ and 5 are presented in Fig. 6. For the round vortex in Fig. 6(a), the most deviated

https://doi.org/10.1121/10.0025138

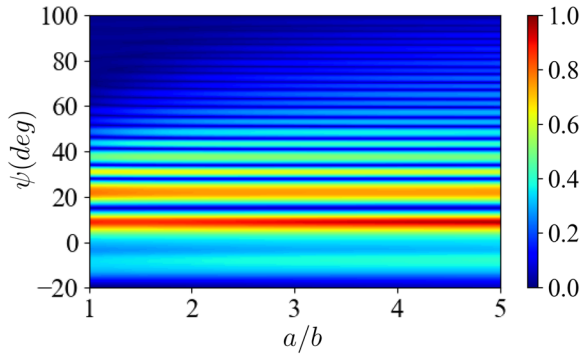

FIG. 5. (Color online) Variations of $|p'_{rms} - p'_{ref,rms}|/p'_{ref,rms}$ as a function of a/b and ψ for a vortex with an orientation angle $\theta = \pi/4$, a maximal Mach number $M_v = 0.15$, and for an acoustic wavelength $\lambda_0/r_0 = 1$.

rays are those passing through the center of the vortex. For the elliptic vortex in Fig. 6(b), the deviation of the rays passing through the center is weaker than for the round vortex.

On the contrary, the rays passing near the vertices of the elliptic vortex are more refracted for $a/b = 5$ than any ray in Fig. 6(a). This is consistent with the increase in the scattering angle with a/b observed in Figs. 4 and 5. The stronger deviation of the rays passing near the vertices of the vortex is due to the variations of the derivatives of the vortex velocity field. As seen in Eq. (5), the time derivative

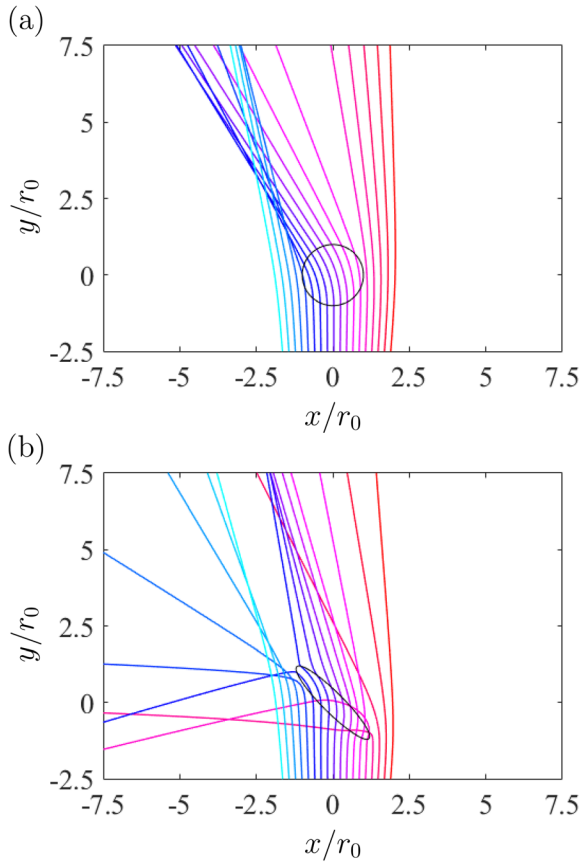

FIG. 6. (Color online) Ray trajectories for (a) $a/b = 1$ and (b) $a/b = 5$ for a vortex with an orientation angle $\theta = \pi/4$, a maximal Mach number $M_v = 0.15$, and for an acoustic wavelength $\lambda_0/r_0 = 1$.

of the wave vector is proportional to the product between the vortex velocity gradient and the wave vector. Thus, the regions with stronger velocity gradients are likely to cause more significant changes in the wave vector direction. As the value of a/b increases, the maximal gradient of the velocity field becomes more important near the vertices of the vortex core. This explains the increase in the angle of refraction near the vertices when the vortex is more elongated. Since the acoustic waves are scattered at greater angles ψ, they overlap with the waves coming directly from the source, generating constructive and destructive interferences far at the left of the vortex. The thinner interference beams obtained at greater angles ψ can also be explained by the fact that at such angles, the angle between the directions of propagation of the scattered and direct waves is larger. Finally, the angular range containing the beams in Fig. 6(a) is narrower than the one in Fig. 5 for $a/b = 1$. This difference may be explained by the ray tracing assumption that $\lambda_0/r_0 \ll 1$, while the simulation of Fig. 5 are performed for $\lambda_0/r_0 = 1$.

B. Influence of the vortex orientation θ

The effects of the vortex orientation θ on the scattering of the sound waves are discussed in this section. The vortex has a Mach number $M_v = 0.15$, a radius such that $\lambda_0/r_0 = 1$, and an aspect ratio $a/b = 3$. Simulations are performed for the range of vortex orientations $-\pi \le \theta \le \pi$.

The levels of $|p'_{rms} - p'_{ref,rms}|/p'_{ref,rms}$ are displayed in Fig. 7 as a function of the orientation angle θ and the observation angle ψ. Because of the geometry of the vortex, the interference patterns have a π-periodicity with θ. The angular positions ψ and the widths of the interference beams do not change much with the angle θ. The two main beams are found around $\psi = 10^\circ$ and $\psi = 20^\circ$. Their amplitudes vary with the angle θ. In particular, the amplitude of the beam at $\psi = 10^\circ$ is maximal for $\theta = \pm\pi/4$ and $\theta = \pm 3\pi/4$. Its minimal amplitude is reached for $\theta = 0$ and $\theta = \pm\pi$. The amplitude of the beam centered around $\psi = 20^\circ$ is also lowest around $\theta = 0$ and $\theta = \pm\pi$. In addition, several narrow beams

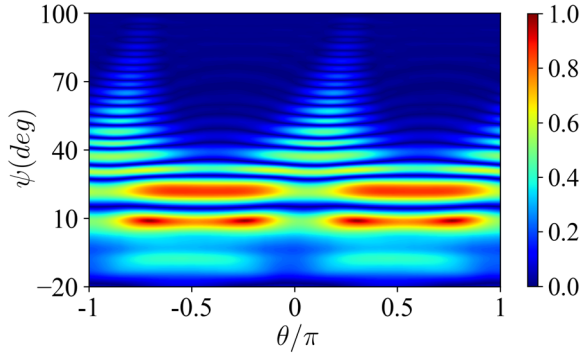

FIG. 7. (Color online) Variations of $|p'_{rms} - p'_{ref,rms}|/p'_{ref,rms}$ as a function of the vortex orientation θ and the observation angle ψ for a vortex with an aspect ratio $a/b = 3$, a maximal Mach number $M_v = 0.15$, and for an acoustic wavelength $\lambda_0/r_0 = 1$.

with low amplitudes are visible for $\psi > 40°$, but only for values of θ roughly between 0 and $\pi/4$.

To explain the present results, the paths followed by acoustic rays have been calculated using the ray tracing method described previously, for an elliptic vortex with $a/b = 3$ and $M_v = 0.15$. The rays obtained for the vortex orientation angles $\theta = \pi/4$ and $\theta = \pi/2$ are presented in Fig. 8. For $\theta = \pi/4$ in Fig. 8(a), the most refracted rays are deviated approximately by 100°. For $\theta = \pi/2$ in Fig. 8(b), as the vortex is oriented horizontally, the rays are poorly affected by the vortex. In this case, the angle of refraction for all rays is lower than 10°. The strong dependency of the deviation of the rays with the vortex orientation angle is due to the vector-matrix product between the wave vector and the vortex velocity gradient in Eq. (5). The wave vector in Eq. (5) verifies that $k_x \simeq 0$ and then the time derivative of the wave vector is parallel to $(\partial v_0/\partial x, \partial v_0/\partial y)$. Thus, for the case $\theta = \pi/2$, the time derivative is vertical near the vertices of the vortex and almost zero elsewhere, meaning that the direction of the wave vector does not vary anywhere. This explains the weak scattering angle for the vortex with $\theta = \pi/2$.

C. Influence of the vortex Mach number *M*

In this section, the influence of the vortex Mach number M_v is investigated. Round vortices and elliptic ones with $a/b = 3$ and $\theta = \pi/4$ are considered for values of M_v ranging from 0 and 0.5. The ratio λ_0/r_0 is equal to 1.

The levels of $|p'_{rms} - p'_{ref,rms}|/p'_{ref,rms}$ are plotted in Fig. 9 as a function of the vortex Mach number M_v and the observation angle ψ. Similar patterns are obtained for the round and the elliptic vortices. The interference beams take the form of lobes existing within limited ranges of Mach numbers. Four dominant lobes are observed around $\psi = 0$, vertically above the vortex. They are oriented towards higher observation angles as the vortex Mach number increases. Lobes are also found at large angles $\psi > 0$ on the left of the vortex. However, they are more numerous and appear over a much wider range of angles ψ for a higher Mach number. In addition, for large observation angles, there are more numerous but less intense lobes for the elliptic vortex in Fig. 9(b) than for the round vortex in Fig. 9(a). For a given Mach number, they reach higher observation angles for the elliptic vortex, as was reported in Sec. IV A.

As previously, the ray tracing method has been used to compute the paths of the acoustic rays passing through the vortex. The rays obtained for $M_v = 0.05$ and $M_v = 0.25$ are shown in Figs. 10(a) and 10(b), respectively. In both cases, the most deviated rays are those passing near the vertices of the vortex. The maximum deviation angles, however, strongly increase with M_v, from approximately 10° for $M_v = 0.05$ up to 115° for $M_v = 0.25$. This result explains the increase in the number of interference beams for large observation angles as the vortex Mach number is higher in Fig. 9.

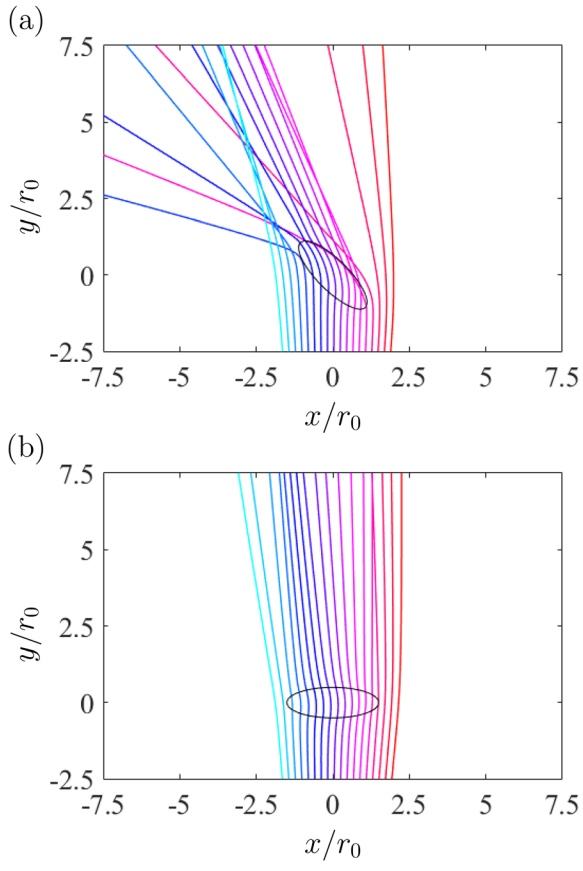

FIG. 8. (Color online) Rays trajectories obtained for (a) $\theta = \pi/4$ and (b) $\theta = \pi/2$ for a vortex with an aspect ratio $a/b = 3$ and a maximal Mach number $M_v = 0.15$.

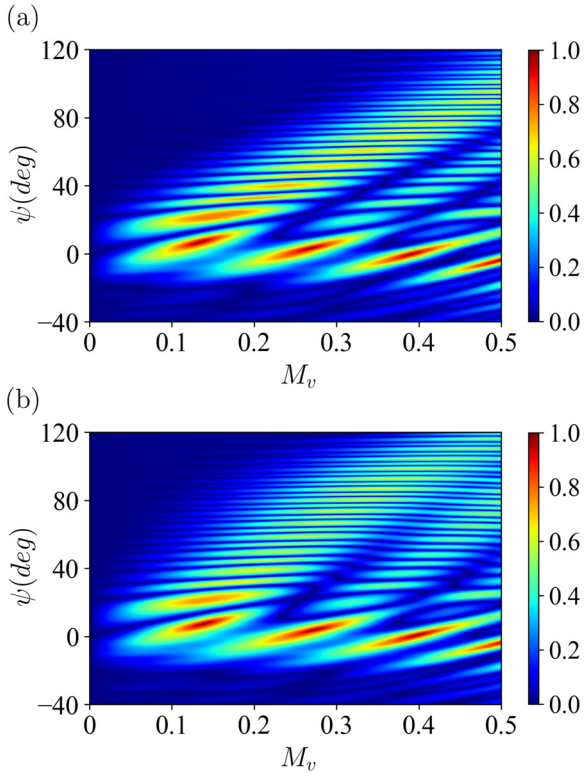

FIG. 9. (Color online) Variations of $|p'_{rms} - p'_{ref,rms}|/p'_{ref,rms}$ as a function of M_v for (a) $a/b = 1$ and (b) $a/b = 3$ for a vortex with an orientation angle $\theta = \pi/4$ and for an acoustic wavelength $\lambda_0/r_0 = 1$.

https://doi.org/10.1121/10.0025138

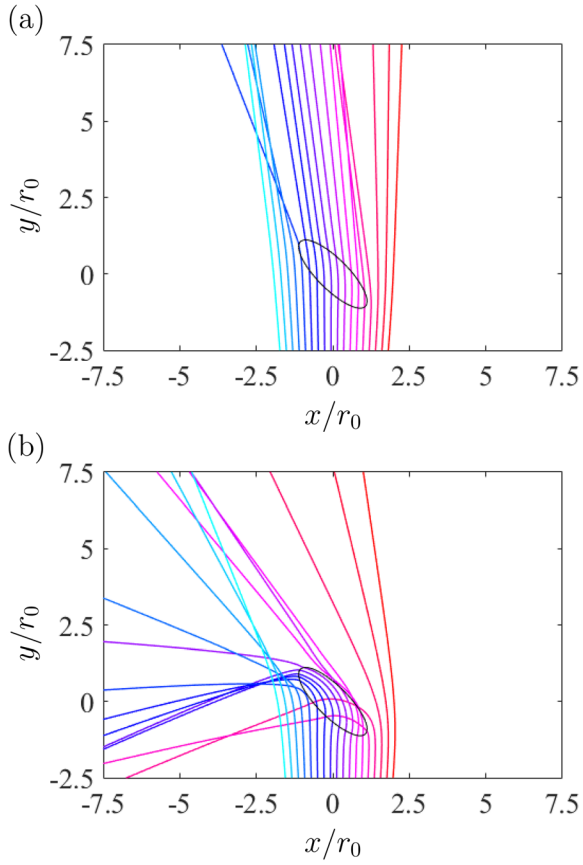

FIG. 10. (Color online) Ray trajectories obtained for (a) $M_v = 0.05$ and (b) $M_v = 0.25$ for a vortex with an aspect ratio $a/b = 3$ and an orientation angle $\theta = \pi/4$.

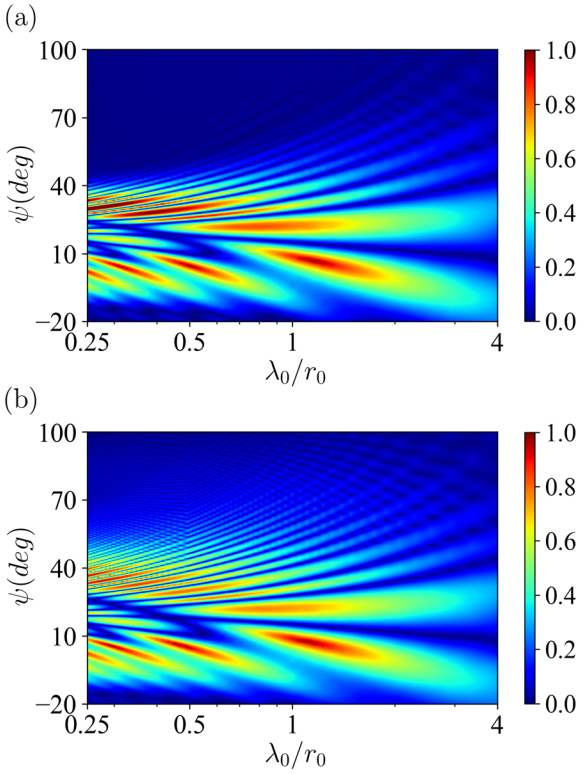

FIG. 11. (Color online) Variations of $|p'_{rms} - p'_{ref,rms}|/p'_{ref,rms}$ as a function of λ_0/r_0 for (a) $a/b = 1$, (b) $a/b = 3$ for a vortex with an orientation angle $\theta = \pi/4$ and a maximal Mach number $M_v = 0.15$.

D. Influence of the acoustic wavelength λ_0

Finally, the effects of the ratio between the acoustic wavelength λ_0 and the size of the vortex r_0 are studied. The ratio between the acoustic wavelength and the vortex size r_0 varies between 1/4 and 4. A round vortex and an elliptic vortex with $a/b = 3$ and $\theta = \pi/4$ are considered. Both have a Mach number $M_v = 0.15$.

Colormaps of $|p'_{rms} - p'_{ref,rms}|/p'_{ref,rms}$ are plotted in Fig. 11 as a function of the wavelength λ_0/r_0 and the observation position ψ. The distributions of the interference beams are similar for the round and elliptic vortices. For values of λ_0/r_0 lower than 0.5, the scattered field consists of a large number of narrow but intense interference beams. For values of λ_0/r_0 greater than 1, the interference beams are much weaker and only a few wide beams are visible. This trend is consistent with the results of existing works.[14] For $\psi > 10°$, the lobes are oriented upwards. Therefore, in this case, the interference beams shift to greater angles ψ when the wavelength increases. For $\psi < 10°$, on the contrary, the lobes are oriented downward indicating a shift of the beams to lower angles ψ. In general, the interference lobes seem to widen with the acoustic wavelength λ_0. Note that, as the wavelength λ_0 is larger than the vortex radius, especially when $\lambda_0 \geq 2r_0$, the geometry of the vortex does not have much influence on the scattered field. On the contrary, when $\lambda_0/r_0 \leq 0.5$, more beams of lower amplitude are observed for the elliptic vortex than for the round one. The sound is also scattered for larger observation angles for the elliptic vortex, as mentioned previously.

V. VORTEX CONVECTED BY A UNIFORM FLOW

In this section, the vortex is convected in the x-direction by a uniform flow. The convection Mach number M_c and the aspect ratio of the vortex vary. As shown in Fig. 3, the vortex is located at $y = 0$ and its major axis is parallel to the x-direction. This choice has been made because the turbulent structures in a shear layer are typically stretched in the flow direction.[18] The monopolar source, located at $x = 0$, $y/r_0 = -25$, emits at a frequency such that $\lambda_0/r_0 = 1$ in a medium at rest and the vortex Mach number is $M_v = 0.15$. The scattering of acoustic waves by a round convected vortex was also investigated in Clair and Gabard[14] for a Gaussian vortex.

A. Spatial scattering

The pressure fields obtained for a round vortex and an elliptic vortex with $a/b = 3$ convected at a Mach number $M_c = 0.3$ when the vortex is located at $x/r_0 = -30$, 0, and 30 are presented in Fig. 12. The convection effects of the uniform flow on the acoustic waves are clearly visible, yielding shorter wavelengths and higher amplitudes upstream of the source, and larger wavelengths and lower

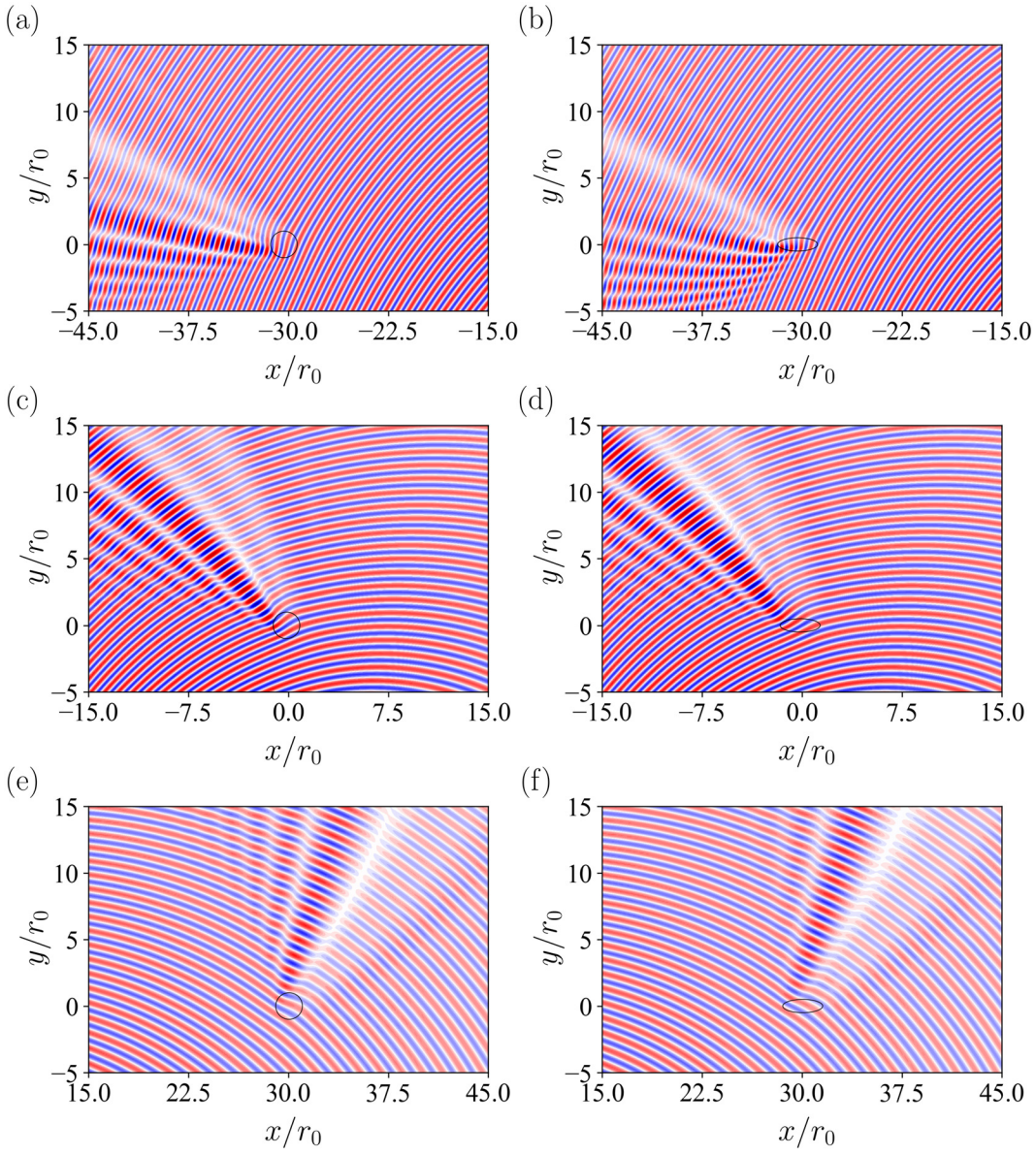

FIG. 12. (Color online) Pressure fields p' obtained for a vortex convected at a Mach number $M_c = 0.3$, when the vortex is located at (a) and (b) $x/r_0 = -30$, (c) and (d) $x = 0$, and (e) and (f) $x/r_0 = 30$: (a), (c,) (e), round vortex, and (b), (d), (f), elliptic vortex with $a/b = 3$, maximal vortex Mach number $M_v = 0.15$ and acoustic wavelength in a medium at rest $\lambda_0/r_0 = 1$.

amplitudes downstream. The interference patterns due to the scattering of the acoustic waves by the vortex differ for the three positions. As the vortex is convected downstream, the interference patterns rotate clockwise because the incidence angle of the acoustic waves on the vortex varies. The number, width, and angular range of the interference beams also change with the position of the vortex. These changes can be attributed to the differences in the orientation of the incident wavefronts and in the wavelength, whose effects are illustrated in Secs. IV B and IV D, respectively. Indeed, the angle between the direction of the incident waves and the direction of the vortex major axis varies from $\theta \simeq 0$ when the vortex is far upstream up to $\theta \simeq \pi$ when it is far downstream. At the same time, the acoustic wavelength varies nearly between $\lambda_0(1 - M_c)$ and $\lambda_0(1 + M_c)$. Thus, a large number of narrow interference beams appears over a wide angular range in Figs. 12(a) and 12(b), while the number of beams is smaller and they extend over a more limited angular range in Figs. 12(e) and 12(f). The results obtained for the two vortex geometries are very similar when the vortex is just above the source in Figs. 12(c) and 12(d), but show slight differences in the two other cases. More precisely, when the vortex is located upstream, additional interference beams are observed for large observation angles $\psi > 0$ for the elliptic vortex in Fig. 12(b) compared with the round vortex in Fig. 12(a), whereas less beams are found when the vortex is downstream in Fig. 12(f) than in Fig. 12(e).

The effects of the convection Mach number M_c are then investigated. For that, the pressure fields obtained for

https://doi.org/10.1121/10.0025138

$M_c = 0$, $M_c = 0.3$ and $M_c = 0.6$ are displayed in Figs. 13(a) and 13(b), 13(c) and 13(d), and 13(e) and 13(f), respectively, when the incident wavefronts impinge perpendicularly to the direction of the vortex major axis. In all cases, this happens when the center of the vortex is located at $x/r_0 = 25M_c$. The results are very similar for the round and the elliptic vortices. When the vortex is in motion, the interference beams are curved, as previously seen in Fig. 12, due to the clockwise rotation of the angle of incidence of the acoustic waves on the vortex. The curvature is more marked for a higher convection Mach number as the vortex travels more rapidly. In addition, more numerous but narrower interference beams are observed, as the acoustic wavelength decreases upstream with the convection Mach number.

B. Spectral broadening

1. Time signals

The pressure field scattered by a convected elliptic vortex is first analyzed from the time signals recorded at the two positions $(x/r_0 = -30, y/r_0 = 16)$ and $(x/r_0 = 30, y/r_0 = 16)$.

The signals obtained at the upstream position for an elliptic vortex with $a/b = 3$ and $M_v = 0.15$, are presented in Fig. 14 for convection Mach numbers $M_c = 0.3$ and 0.6. They are plotted as a function of t/t_{M_c}, where $2t_{M_c}$ is the time taken by the vortex to travel through the physical domain. Thus, the vortex enters the domain at $t = -t_{M_c}$, is located at $x = 0$ at $t = 0$, and exits at $t = t_{M_c}$. For both $M_c = 0.3$ and 0.6, the signals exhibit amplitude modulation due to the interference beams passing over the observation

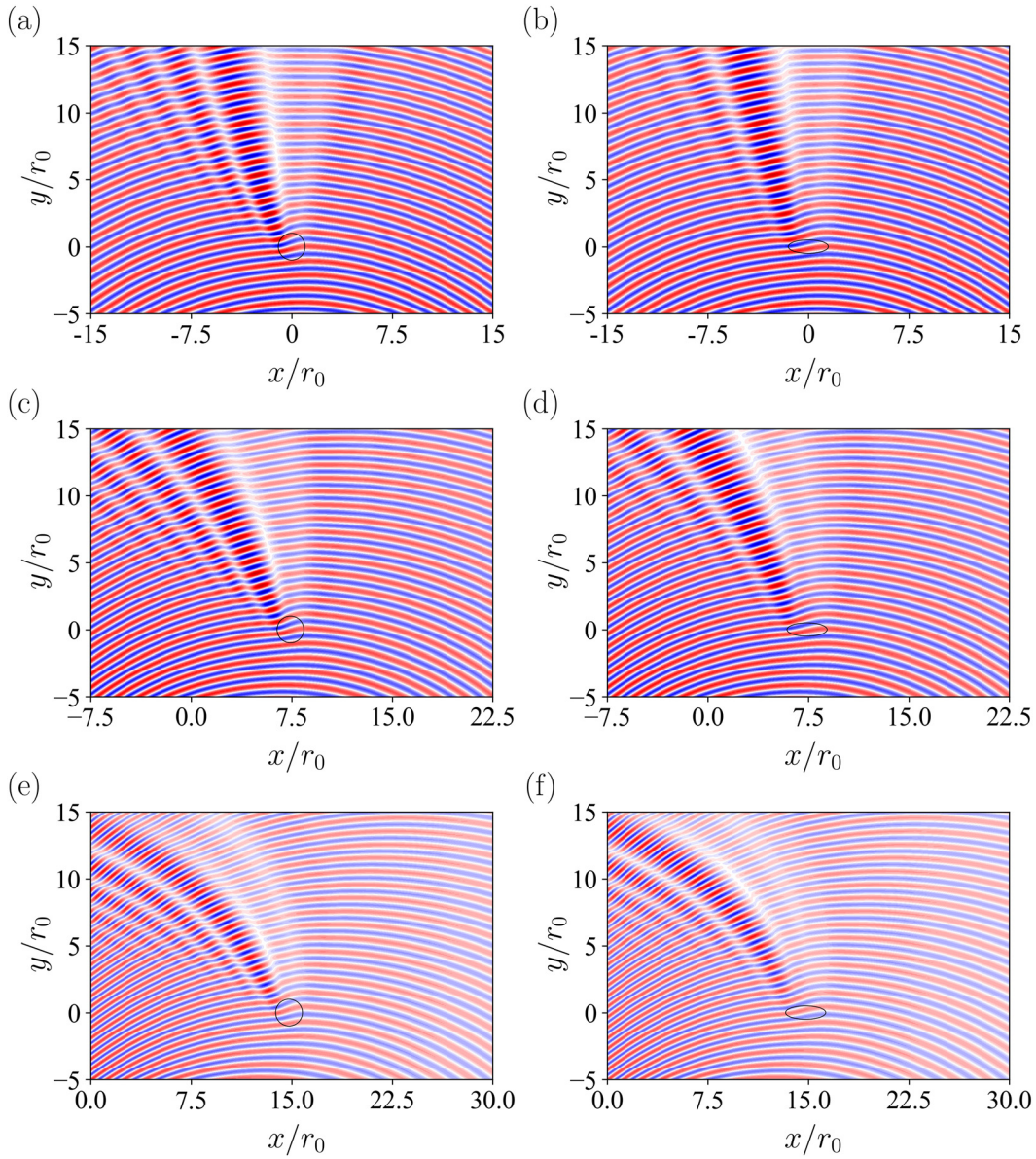

FIG. 13. (Color online) Pressure fields p' obtained for a vortex convected at a Mach number (a) and (b) $M_c = 0$, (c) and (d) $M_c = 0.3$, and (e) and (f) $M_c = 0.6$: (a) (c), (e) round vortex, and (b), (d), and (f) elliptic vortex with $a/b = 3$, maximal vortex Mach number $M_v = 0.15$ and acoustic wavelength in a medium at rest $\lambda_0/r_0 = 1$.

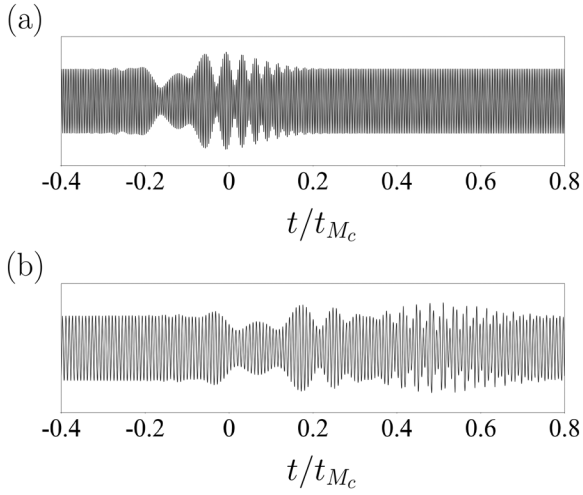

FIG. 14. Pressure signal at $x/r_0 = -30$ and $y/r_0 = 16$ for an elliptic vortex with an aspect ratio $a/b = 3$ and a maximal Mach number $M_v = 0.15$ convected at Mach number (a) $M_c = 0.3$, (b) $M_c = 0.6$, for an acoustic wavelength $\lambda_0/r_0 = 1$.

position. In Fig. 14(a), for $M_c = 0.3$, the modulations occur between $-0.2 \leq t/t_{M_c} \leq 0.2$ and can be related to the interference beams visible in the pressure field in Fig. 12(b). In Fig. 14(b) for $M_c = 0.6$, the modulation pattern is relatively similar to that in Fig. 14(a), but appears later since the interference beams are trailing further behind the vortex for $M_c = 0.6$ than for $M_c = 0.3$, as shown in Fig. 13.

The signals obtained downstream at $x/r_0 = 30$ and $y/r_0 = 16$ for $M_c = 0.3$ and $M_c = 0.6$ are plotted in Fig. 15. The amplitude modulations are visible over a shorter time period, and the number of modulations is smaller than at the upstream observation point in Fig. 14. This is due to a smaller number of interference beams downstream than upstream, as is visible in Fig. 12. The modulations appear latter for $M_c = 0.6$ than for $M_c = 0.3$ as in Fig. 14, but the time shift is less important than for the upstream signals.

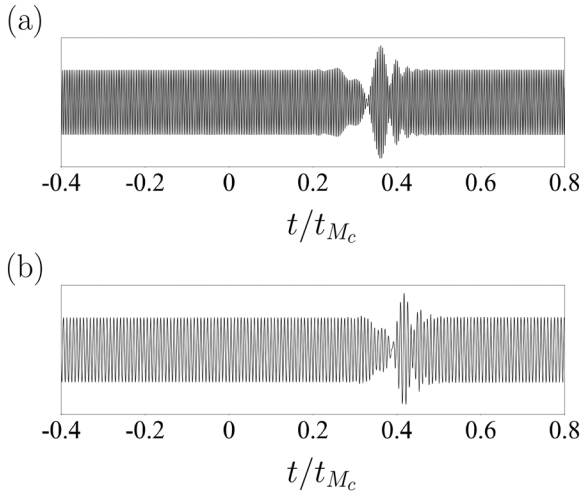

FIG. 15. Pressure signal at $x/r_0 = 30$ and $y/r_0 = 16$ for an elliptic vortex with an aspect ratio $a/b = 3$ and a maximal Mach number $M_v = 0.15$ convected at Mach number (a) $M_c = 0.3$, (b) $M_c = 0.6$, for an acoustic wavelength $\lambda_0/r_0 = 1$.

2. Spectral densities

The power spectral densities (PSD) of the pressure fluctuations have been calculated using the signals recorded at $y/r_0 = 16$ and $x/r_0 = -30$, 0, and 30 between $t = -t_{M_c}$ and $t = t_{M_c}$.

These PSD obtained for a round vortex and an elliptic vortex with $a/b = 3$, for $M_v = 0.15$, $M_c = 0.3$, and $\lambda_0/r_0 = 1$, are plotted in Fig. 16 as a function of the centered normalized frequency $(f - f_0)r_0/(M_c c_0)$. The spectra show a

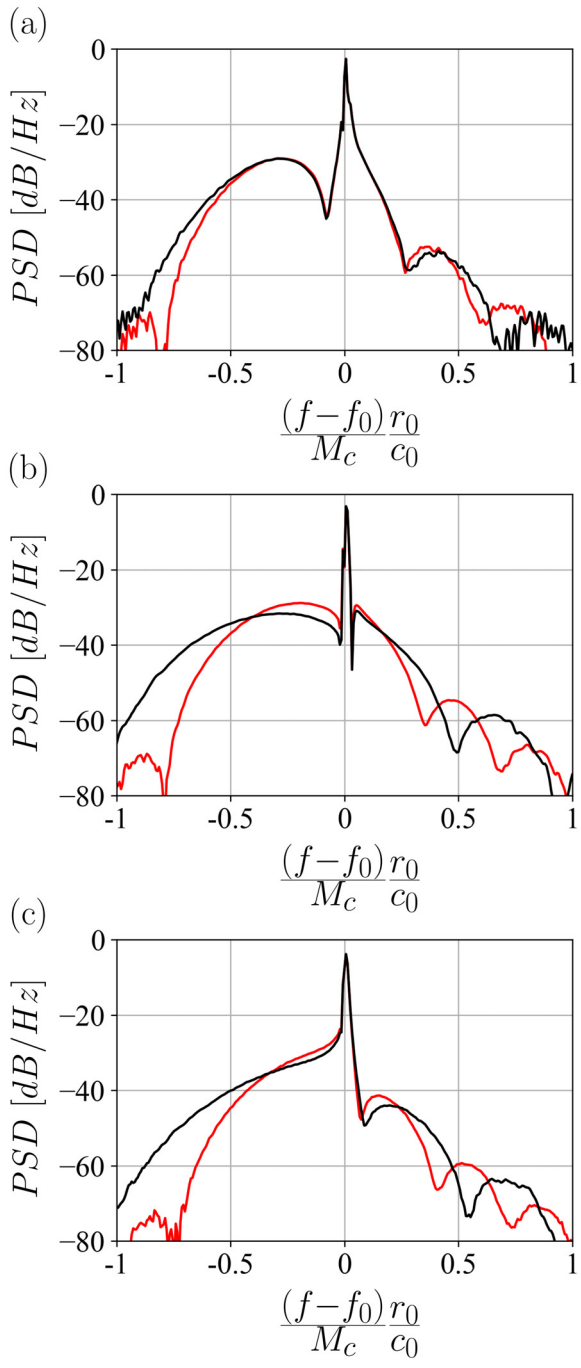

FIG. 16. (Color online) PSD levels obtained at (a) $x/r_0 = -30$, (b) $x = 0$, and (c) $x/r_0 = 30$, $y/r_0 = 16$ for $M_c = 0.3$ and (black solid line) $a/b = 1$ and (red solid line) $a/b = 3$. The other parameters are the maximal Mach number $M_v = 0.15$ and the acoustic wavelength $\lambda_0/r_0 = 1$.

https://doi.org/10.1121/10.0025138

central peak at $f=f_0$, and sidelobes on both sides corresponding to the energy shifted from f_0 due to Doppler effects resulting from the scattered field radiated by the moving vortex. The existence of lobes in the scattered pressure field gives rise to sidelobes on the PSD. The frequency shift of a sidelobe is larger for lobes that are located further away from $\psi = 0°$. Overall, similar trends are found for the round and the elliptic vortices. A single large lobe is observed for $f < f_0$, while several narrower lobes are noted for $f > f_0$. As the observer position moves downstream, the lobe at $f < f_0$ becomes wider and its maximum gets closer to f_0, to even disappear in Fig. 16(c) for $x/r_0 = 30$. The maximum values of the lobes at $f > f_0$ are reached at higher frequencies. Regarding the differences between the round and the elliptic vortices, the sidelobes are significantly narrower for the elliptic vortex, for example in Fig. 16(b), yielding maxima closer to each other. In particular, the maxima of the first lobes on both sides of the central peak at $f=f_0$ are closer to the source frequency.

The spectra obtained for the same vortices and acoustic wavelength as in Fig. 16, but with a convection Mach number $M_c = 0.6$ instead of $M_c = 0.3$, are presented in Fig. 17. The results are similar in the two Figs. 16 and 17. This is particularly the case in Fig. 16(c) and Fig. 17(c) downstream of the source. Upstream and above the source, however, differences can be noted as the convection Mach number varies. The sidelobes are narrower for $M_c = 0.6$ than for $M_c = 0.3$. At $x/r_0 = -30$, in addition, they reach their maximum values at different frequencies for the round and the elliptic vortices in Fig. 17(a), which was not the case in Fig. 16(a).

VI. CONCLUSIONS

In this work, the scattering of acoustic waves by an elliptic vortex is investigated with the aim of understanding the effects of the parameters defining the vortex, especially those unique to elliptic vortices, such as the aspect ratio and the orientation with regard to the incident wavefronts. The velocity magnitude of the vortex and its size relative to the incident acoustic wavelength are also studied.

In the first section, the effects of each of the first four parameters were investigated separately for a stationary vortex scattering the acoustic waves radiated by a monopole. The vortex aspect ratio appears to have a weak effect on the scattered field. In particular, for the orientation angle $\theta = \pi/4$, a more elliptic vortex leads mostly to the appearance of additional, low amplitude interference beams at large observation angles. This is due to the refraction of the acoustic waves towards greater angles because the velocity gradient increases with the ellipticity of the vortex. The vortex orientation has a significant influence on the amplitude and the angular range of interference beams because the angle between the velocity gradient and the incident wave vector affects the deviation of the wave direction. This deviation is minimal when the elliptic vortex major axis is aligned perpendicularly to the wave direction. The effects of

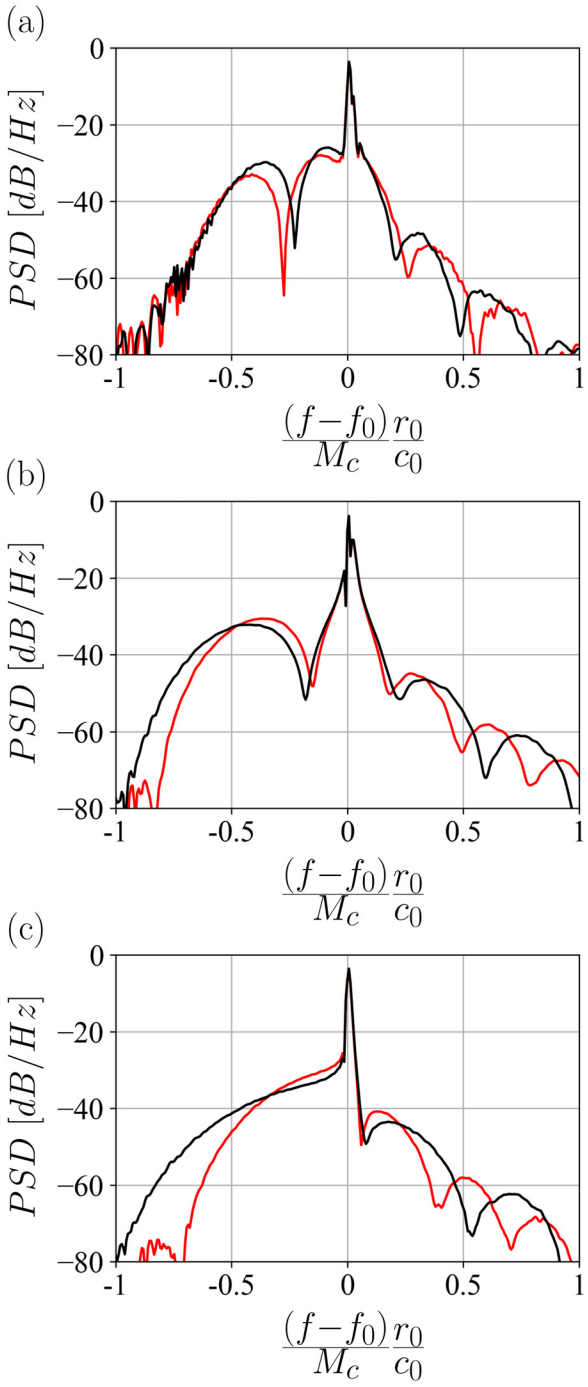

FIG. 17. (Color online) PSD levels obtained at (a) $x/r_0 = -30$, (b) $x=0$, and (c) $x/r_0 = 30$, $y/r_0 = 16$ for $M_c = 0.6$ and (black solid line) $a/b = 1$ and (red solid line) $a/b = 3$. The other parameters are the maximal Mach number $M_v = 0.15$ and the acoustic wavelength $\lambda_0/r_0 = 1$.

the Mach number are similar for the round vortex and the elliptic vortex. However, for a given Mach number, additional interference beams are observed at large observation angles when the vortex is elliptic.

In the second section, the vortex was convected by a uniform mean flow. The effect of the ellipticity, the position, and the convection Mach number of the vortex were studied. Because of the convection, the elliptic vortex orientation

evolves while the vortex is traveling. As a result, differences between the elliptic and round vortices can be observed in the interference patterns, with more interference beams for the elliptic vortex when it is located upstream, and less when it is located downstream. These differences are consistent with the observations made on the effects of the parameters of the elliptic vortex at a fixed position. Finally, the spectra obtained upstream, vertically, and downstream of the source present similarities, with sidelobes around the source frequency associated with the scattered field and a Doppler shift, as described in previous work for round vortices. Nevertheless, the differences observed in the interference patterns for the pressure fields result in sidelobes that appear narrower for the elliptic vortex, with maxima that are located closer to the source frequency.

ACKNOWLEDGMENTS

This work is funded by Siemens Digital Industries Software through the Ph.D. program CIFRE 2021/0106. It was granted access to the HPC resources of PMCS2I (Pôle de Modélisation et de Calcul en Sciences de l'Ingénieur de l'Information) of École Centrale de Lyon. The authors would like to acknowledge S. Le Bras for her close and careful supervision of this work. For the purpose of Open Access, a CC-BY public copyright license has been applied by the authors to the present document and will be applied to all subsequent versions up to the author-accepted manuscript arising from this submission.

AUTHOR DECLARATIONS

Conflict of interest

The authors report no conflict of interest.

DATA AVAILABILITY

Data from numerical simulations are available from the authors on reasonable request.

[1]S. Candel, A. Guedel, and A. Julienne, "Radiation, refraction and scattering of acoustic waves in a free shear flow," AIAA Paper 76-544 (1976).
[2]S. Candel, A. Guedel, and A. Julienne, "Résultats préliminaires sur la diffusion d'une onde acoustique par écoulement turbulent" ("Preliminary results on the diffusion of an acoustic wave by a turbulent flow") J. Phys. Colloq. **37**, C1-153–160 (1976).
[3]S. Candel, A. Julienne, and A. Guedel, "Refraction and scattering of sound in an open wind tunnel flow," in *Proceedings of ICIASF'75; 6th International Congress on Instrumentation in Aerospace Simulation Facilities*, Ottawa, Canada (September 22–24, 1975), pp. 288–300.
[4]I. Bennaceur, D. C. Mincu, I. Mary, M. Terracol, L. Larchevêque, and P. Dupont, "Numerical simulation of acoustic scattering by a plane turbulent shear layer: Spectral broadening study," Comput. Fluids **138**, 83–98 (2016).
[5]R. Ewert, "RPM - the fast random particle-mesh method to realize unsteady turbulent sound sources and velocity fields for CAA applications," AIAA Paper 2007-3506 (2007).
[6]T. Suzuki, "Coherent noise sources of a subsonic round jet investigated using hydrodynamic and acoustic phased-microphone arrays," J. Fluid Mech. **730**, 659–698 (2013).
[7]T. Colonius, S. Lele, and P. Moin, "The scattering of sound waves by a vortex: Numerical simulations and analytical solutions," J. Fluid Mech. **260**, 271–298 (1994).
[8]J. H. Ferziger, "Low-frequency acoustic scattering from a trailing vortex," J. Acoust. Soc. Am **56**(6), 1705–1707 (1974).
[9]R. Ford and S. G. Llewellyn Smith, "Scattering of acoustic waves by a vortex," J. Fluid Mech. **386**, 305–328 (1999).
[10]S. O'Shea, "Sound scattering by a potential vortex," J. Sound Vib. **43**(1), 109–116 (1975).
[11]J. E. Yates, "Application of the Bernoulli enthalpy concept to the study of vortex noise and jet impingement noise," NASA-CR-2987 (NASA, Washington, DC, 1978).
[12]S. Candel, "Numerical solution of conservation equations arising in linear wave theory: Application to aeroacoustics," J. Fluid Mech. **83**(3), 465–493 (1977).
[13]V. Clair and G. Gabard, "Numerical assessment of the scattering of acoustic waves by turbulent structures," AIAA Paper 2015-2680 (2015).
[14]V. Clair and G. Gabard, "Spectral broadening of acoustic waves by convected vortices," J. Fluid Mech. **841**, 50–80 (2018).
[15]T. M. Georges, "Acoustic ray paths through a model vortex with a viscous core," J. Acoust. Soc. Am **51**(1B), 206–209 (1972).
[16]E. Kam, R. So, S. C. Fu, and R. Leung, "Finite difference lattice Boltzmann method applied to acoustic-scattering problems," AIAA J. **48**(2), 354–371 (2010).
[17]R. Ma, Y. Wang, H. Li, C. Wu, S. Han, and X. Wang, "Numerical study on the scattering of acoustic waves by a compact vortex," Phys. Fluids **35**(3), 036107 (2023).
[18]D. W. Moore and P. G. Saffman, "The density of organized vortices in a turbulent mixing layer," J. Fluid Mech. **69**, 465–473 (1975).
[19]H. Lamb, *Hydrodynamics* (Cambridge University Press, Cambridge, UK, 1932).
[20]S. Barré, C. Bogey, and C. Bailly, "Direct simulation of isolated elliptic vortices and of their radiated noise," Theor. Comput. Fluid Dyn. **22**, 65–82 (2008).
[21]M. E. Goldstein, *Aeroacoustics* (McGraw-Hill International Book Co., New York, 1976).
[22]J. S. Hesthaven and T. Warburton, *Nodal Discontinuous Galerkin Methods: Algorithms, Analysis, and Applications* (Springer-Verlag, New York, 2008).
[23]M. Williamschen, G. Gabard, and H. Beriot, "Performance of the DGM for the linearized Euler equations with non-uniform mean-flow," AIAA Paper 2015-3277 (2015).
[24]C. Bogey and C. Bailly, "A family of low dispersive and low dissipative explicit schemes for flow and noise computations," J. Comput. Phys. **194**, 194–214 (2004).
[25]M. Williamschen, "Time-domain DGM for turbofan exhaust noise predictions," Ph.D. thesis, (University of Southampton, Southampton, UK, 2018).
[26]P. Sijtsma, S. Oerlemans, T. G. Tibbe, T. Berkefeld, and C. Spehr, "Spectral Broadening by Shear Layers of Open Jet Wind Tunnels," AIAA paper 2014-3178 (2014).